

Dynamics of the Cumulus Cloud Margin: An Observational Study

YONGGANG WANG, BART GEERTS, AND JEFFREY FRENCH

University of Wyoming, Laramie, Wyoming

(Manuscript received 4 March 2009, in final form 1 July 2009)

ABSTRACT

Aircraft observations of shallow to moderately deep cumulus clouds are analyzed with the purpose of describing the typical horizontal structure of thermodynamic and kinematic parameters near the cumulus margin from the cloud center into the ambient clear air. The cumuli were sampled in a broad range of environments in three regions: the tropical Atlantic Ocean in winter, the Sonoran Desert during the monsoon, and the arid high plains of Wyoming in summer. The composite analysis of 1624 cumulus penetrations shows that the vertical mass flux, temperature, buoyancy, the buoyancy flux, and the turbulent kinetic energy all tend to reach a minimum near the cloud edge. Most of these variables, and also the liquid water content, the droplet concentration, and the mean droplet size, generally decrease in value from within the cumulus toward the cloud edge, slowly at first and rapidly close to the cloud edge. These findings corroborate recent observational and modeling studies and provide further evidence for significant evaporative cooling in laterally entraining and detrainning eddies in the cloud margin, a transition zone within ~ 200 m (or $\sim 10\%$ of the cloud diameter) of the cloud edge. This cooling explains the tendency for downward accelerating, buoyantly driven subsidence in the cloud margin.

1. Introduction

Cumulus clouds are important in the earth system as they affect the vertical structure of tropospheric radiative heat flux divergence and dynamically couple the planetary boundary layer to the free troposphere through the vertical transport of heat, moisture, aerosol, and momentum (e.g., Siebesma et al. 2003). Cumulus cloud circulations are smaller than resolvable scales in numerical weather prediction (NWP) and general circulation models (e.g., Kharoutdinov et al. 2008) and they occur in a broad range of vertical and horizontal scales (e.g., Lopez 1977; Wielicki and Welch 1986). Cumulus clouds are the main source of precipitation at low latitudes and during the warm season at higher latitudes. It is largely because the subgrid-scale vertical transport by cumulus convection is inadequately presented in NWP models that precipitation is less predictable in the warm season than the cold season (e.g., Carbone et al. 2002; Weckwerth et al. 2004).

Many studies have examined macroscale geometric properties of cumulus clouds (e.g., Sengupta et al. 1990).

These properties are in part controlled by the way that cumuli exchange water and energy with their cloud-free environment. Entrainment of ambient air across the cloud edge fundamentally affects the cloud's dynamics (e.g., Raga et al. 1990; Blyth 1993; Grabowski 1993; Krueger et al. 1997; Carpenter et al. 1998), and detrainment of cloudy air into the surrounding clear air cumulatively alters the environment. While entrainment may affect the structure and evolution of organized deep convection, the focus of the present study is on the scale of individual cumulus towers.

Several recent studies have used large-eddy simulations (LES) to document the kinematics, microphysics, and thermodynamics of individual cumulus towers (e.g., Zhao and Austin 2005a,b; Abel and Shipway 2007; Heus et al. 2008). These studies have afforded very detailed depictions of the mixing process, vertical mass, and energy transfers in cumulus clouds. For decades observational studies have led the way toward understanding cumulus processes, but recently modeling studies have taken the lead. Recent observational studies, including this study, are intended largely to validate model-based findings.

The effect of turbulent mixing of cumuli with their immediate environment has been examined mainly by means of conserved variable diagrams (e.g., Paluch 1979). While such diagrams are useful in the assessment

Corresponding author address: Bart Geerts, Dept. of Atmospheric Sciences, University of Wyoming, Laramie, WY 82071.
E-mail: geerts@uwyo.edu

of vertical and lateral entrainment, they do not describe the characteristic horizontal structure of cloud properties from core to edge, nor the properties of the near-cloud environment. Many studies have displayed cloud edge thermodynamic data collected from individual aircraft penetrations of cumuli (e.g., Warner 1955), but single slices are not very meaningful in a turbulent environment. To our knowledge, Rodts et al. (2003) were the first to composite aircraft data of kinematic, thermodynamic, and cloud parameters from a large number of flight legs through cumuli and their immediate environment.

A striking feature in their composite cross sections is a thin shell of descending air just outside the cloud edge. Rodts et al. (2003) attributed this local subsidence mainly to evaporative cooling resulting from mixing. Local subsidence in the cumulus shell, just ~ 200 m wide, had been noted before by Jonas (1990), using a smaller sample of aircraft penetrations. Jonas (1990) attributed this subsidence to mechanical forcing, rather than evaporative cooling. Recent LES studies have confirmed the presence of cumulus shell subsidence, and have identified evaporative cooling as the main forcing (Zhao and Austin 2005a; Heus and Jonker 2008; Jonker et al. 2008).

In this study, we use aircraft data to examine the variation of vertical velocity, buoyancy, and cloud microphysical properties in the vicinity of the cumulus cloud edge, based on 1624 cumulus samples, to examine how entraining and detraining eddy fluxes affect the typical structure of the cumulus cloud shell. In particular, we examine whether evaporative cooling in the cloud margin leads to negative buoyancy and sinking motion, as suggested by recent LES studies. The composite observations across the cloud edge, presented herein, do not shed insight into the relative significance of vertical versus lateral entrainment, but they do suggest a minimum dimension for buoyant cumuli to survive lateral erosion.

Data sources and the analysis method are introduced in section 2. Section 3 describes the characteristic horizontal structure of cumuli using a normalized distance and stratifies this as a function of flight level in-cloud. Section 4 reexamines the horizontal structure in terms of physical distance from the cloud edge. Section 5 (discussion) revisits the question of whether cloud margin subsidence is driven by evaporative cooling. Section 6 provides the conclusions.

2. Data sources and analysis method

A large number of cumulus clouds (Cu) were penetrated by an instrumented aircraft, the University of Wyoming King Air (WKA), in four recent campaigns. The first two

are collectively referred to as “high plains,” where a total of 95 h were flown in two summertime campaigns in Wyoming—that is, the 2003 high plains cumulus (HiCu-03) campaign (Damiani et al. 2006) and the 2008 cloud-GPS campaign. The “Atlantic trade wind Cu” dataset is based on 89 flight hours targeting more shallow, precipitating cumuli over the tropical North Atlantic Ocean in the rain in cumulus over the ocean campaign (RICO-04), conducted east of the Lesser Antilles islands in winter (Rauber et al. 2007). The “Arizona monsoon” cases are derived from WKA penetrations of shallow to deep orographic convection during summer in Arizona, which is part of the Cumulus Photogrammetric, In Situ, and Doppler Observations campaign (CuPIDO-06) (Damiani et al. 2008; Geerts et al. 2008).

All flight data for the four campaigns were perused for adequate samples of Cu and their immediate environment. The Cu selection criteria are based on the cloud droplet concentration N_d (number of droplets per unit volume), obtained from the forward scattering spectrometer probe (FSSP). The FSSP count can include ice crystals (or crystals shattered upon entering the FSSP), but ice crystal concentrations typically are orders of magnitude smaller than droplet concentrations. The selection criteria are twofold: 1) the cloud (defined as a region with average $N_d > 40 \text{ cm}^{-3}$ in RICO-04, and $N_d > 100 \text{ cm}^{-3}$ in the other campaigns) needs to be at least 200 m wide; 2) no cloud can be present outside this cloud over a distance at least half the cloud width along the flight track. The threshold values for N_d were chosen based on the number of Cu penetrations (“cases”) retained. For instance, for RICO-04, N_d thresholds of 20, 40, 60, and 80 cm^{-3} yielded 624, 549, 124, and 49 good cases, respectively. A threshold of 40 cm^{-3} yields enough cases, yet eliminates those sections (at least 200 m long) with only thin or broken clouds.

The choice of minimum cloud size is a compromise between the desire to maximize the sample size and the requirement that clouds be sufficiently wide to resolve lateral entrainment patterns and to calculate meaningful flux quantities. To a first order the Cu size distribution (based on the N_d thresholds mentioned above) shows a lognormal pattern—that is, the number of clouds decreases roughly exponentially with increasing threshold cloud width. A lognormal pattern corresponds with a linear change of the cumulative frequency with cloud size if the frequency scale is logarithmic (Fig. 1) (Lopez 1977). This applies rather well in the three environments and has been observed elsewhere, mainly based on photographic, satellite, and radar data (e.g., Lopez 1977; Hozumi et al. 1982; Wielicki and Welch 1986). The sampled high plains Cu were relatively large, and the Atlantic trade wind Cu were relatively small. The 200-m

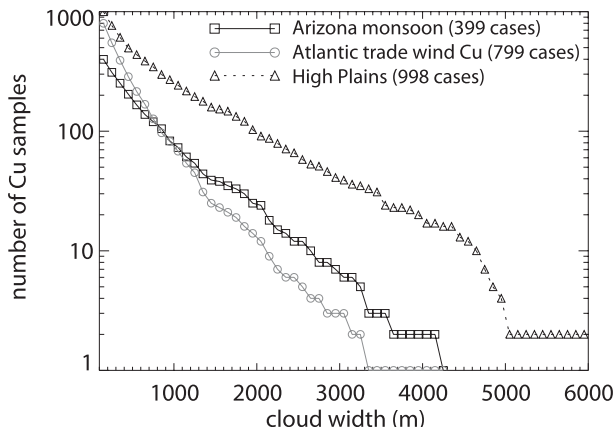


FIG. 1. Cumulative cloud size distribution in three environments. The ordinate shows the number of cases as a function of threshold cloud width.

threshold size yields 1624 samples. Clearly, the sample size rapidly decreases for threshold cloud sizes more than 200 m.

The 1624 Cu samples are characterized in terms of averages and distributions as a function of horizontal distance from the cloud center. All data are redistributed from a time dimension to a distance dimension using the air relative aircraft speed. We examine Cu characteristics as a function of both the actual distance (x) across clouds (section 4) and a normalized distance (x^*) (section 3). The former gives an idea of the physical dimension of lateral exchanges across the cloud edge. The latter, a technique adapted from Rodts et al. (2003), allows an equal number of samples in each distance bin. In both cases, the transects are centered on the cloud edge, therefore $x^* = 0$ at the cloud edge. This defines the term “cloud edge” in this study—that is, the point where $N_d = 0$, as opposed to the term “cloud margin,” which is used herein to refer to the transition region in which lateral entrainment is significant. We set $x^* = -1$ at the cloud center. The composites shown only include data from the center of the cloud to a cloud half-width distance in

the clear air, where $x^* \equiv +1$. For relatively isolated clouds, this implies that two sections are included: the entry and exit parts. But, for most clouds, only one-half can be included, because most sampled Cu towers occurred in clusters and the clear-air region between the towers was too small. Here, we use a bin size Δx^* of 0.05.

In terms of flight direction, both cloud exits and cloud entrances are included. We have contrasted composite cloud exit data against cloud entrance data for a number of variables, to ensure that no measurement bias as a result of flight direction occurred. Temperature is measured by a reverse flow thermometer, which is an immersion probe developed to minimize sensor wetting in-cloud. The comparison between cloud entrance and cloud exit composite temperature traces shows that some probe wetting does occur, and thus also evaporative cooling following exit (Wang and Geerts 2009). The temperature has been corrected for this sensor evaporative cooling bias following Wang and Geerts (2009).

A fast-response water vapor sensor, the LI-COR 6060, was available in only two of the four campaigns (RICO-04 and CuPIDO-06). This sensor displayed wetting symptoms in some Cu penetrations and there is evidence that sometimes, when at temperatures below 0°C, rime accumulated on the sensor, rendering the water vapor trace following cloud exit unreliable. This problem did not occur in RICO-04 (where penetrations were all below the freezing level), but the LI-COR 6060 mixing ratio traces from RICO-04 still show a significant difference between the cloud exit and cloud entrance composites (Fig. 2). This difference is partly due to occasional instrument wetting, but is also a result of the inadequate response time of the sensor, since there appears to be a lag of ~ 0.05 in the exit trace (Fig. 2). Both the evaporation of droplets and the slow instrument response are expected to produce a quasi-exponential adjustment to a step function change. Because of the difference between exit and entrance regions, the LI-COR 6060 data are not used in the composites. Instead, we inferred humidity variables from a chilled mirror dewpoint sensor, which has a much

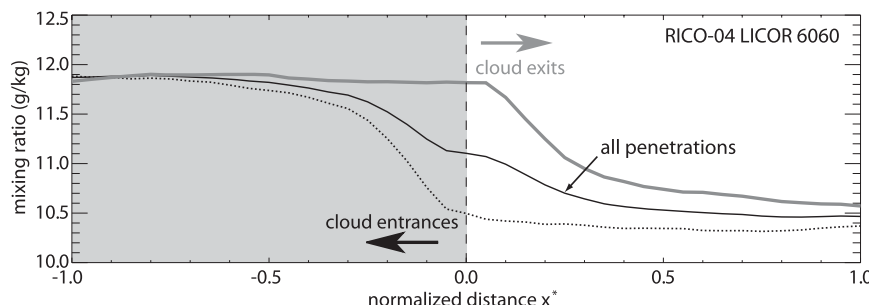


FIG. 2. Effect of flight direction (shown as a bold arrow) on LI-COR 6060 water vapor mixing ratio for all cumulus penetrations in RICO-04 (549 cases). The shaded region is cloudy.

slower response time and is inadequate to describe rapid humidity variations near the cloud edge. For derived variables dependent on humidity, such as buoyancy, we have to assume in-cloud saturation and slowly varying conditions in the clear-air shell, as measured by the chilled mirror dewpoint sensor. Under this assumption, traces of conserved variables, such as total water and wet equivalent potential temperature (e.g., Paluch 1979), show an artificial discontinuity across the cloud edge. Therefore, these otherwise useful variables are not shown.

Vertical and horizontal air velocities are derived from the WKA gust probe (Lenschow et al. 1991). The cloud liquid water content (LWC) is inferred from the FSSP by integrating over all droplet size bins (Brenguier et al. 1994). This integration does not include drizzle or rain drops, but the FSSP LWC generally compares well (within $\sim 10\%$) with the total LWC from the Gerber Particle Volume Monitor (PVM-100; Gerber et al. 1994) and the Droplet Measurement Technologies hotwire probe (DMT-100; King et al. 1981) on the WKA. The mean droplet diameter (D) is also inferred from the FSSP.

The temperature, FSSP, and the gust probe velocity measurements have a frequency of at least 10 Hz. The temperature sensor exhibits some lag to a step function temperature change but it is shorter than 0.1 s (Spyers-Duran and Baumgardner 1983). For the smallest cloud in our sample (with a half-width of 100 m), Δx^* corresponds with 10 m or 8.5 Hz for a typical WKA flight speed of 85 m s^{-1} . This implies that the data frequency is better than the resolution plotted in the normalized distance composites for all 1624 Cu samples. In other words, any smooth or gradual transition of any variable across the cloud edge cannot be attributed to inadequate data sampling frequency or inadequate instrument response time.

For nearly half of the 1624 Cu samples in our database, we were able to determine the cloud base and cloud top. The cloud base is defined as the lifting condensation level (LCL) computed from potential temperature and mixing ratio data mixed in the lowest 50 hPa above the surface, for those cases where soundings were available within ~ 2 h and within a distance of ~ 100 km. Numerous mobile GPS advanced upper-air sounding (MGAUS) radiosondes were launched during flight operations in RICO-04 and CuPIDO-06. Close proximity soundings were not available for the high plains Cu, so we estimated the LCL from temperature and dewpoint data from the nearest operational weather station aircraft data, as well as from aircraft data collected near the ground and usually just after take off and/or just before landing. The cloud base was chosen to be the lowest of the two LCL estimates.

The cloud top is defined as the highest echo seen by the Wyoming Cloud Radar (WCR) above the WKA during Cu penetration. This tends to be an underestimate under the following two conditions: 1) if the aircraft track is not right under the cloud top (e.g., for a tilted or cone-shaped Cu); and 2) if the cloud-top echo is too weak for the WCR to "see." The latter can be the case for shallow, ice-free continental Cu (weak echo) and for deep precipitating Cu (signal attenuation by interspersed precipitation). However, a visual inspection of all cases reveals that the WCR reflectivity is rarely fully attenuated near the top. Sometimes the echoes were too weak, and subsequently the case would be eliminated. In some cases, the cloud top appeared to be above the maximum range of the WCR data (e.g., 3 km above flight level). Even though the multiantenna WCR was operational in all four campaigns, WCR zenith reflectivity profiles simply were not available for many Cu penetrations. In summary, the cloud top could be estimated for 46% of all Cu samples.

3. Horizontal structure of cumuli and their clear-air shell

a. Basic cumulus characteristics

Histograms of the characteristics of the sampled cumulus clouds in the four campaigns are shown in Fig. 3. Clearly, the high plains Cu were the most "continental," with the highest N_d , the lowest LWC, and the smallest mean drop size. These Cu generally had a high cloud base that was sometimes above the freezing level. Many Arizona monsoon Cu had a remarkably high LWC, and in terms of droplet size distribution and N_d the Arizona monsoon Cu was intermediate between the maritime Atlantic trade wind Cu and the truly continental high plains Cu. Most clouds contained some liquid or frozen precipitation, according to the two-dimensional precipitation particle probe (2D-P) and WCR data, with rain reaching the earth surface for most Atlantic trade wind Cu and for some Arizona monsoon Cu.

As will be shown to follow, the sampled cumuli in the three environments were generally of the humilis to congestus type. Cloud depths ranged from a few 100 m to ~ 6000 m. All Atlantic trade wind clouds were relatively shallow clouds with tops below the freezing level (Fig. 3d), whereas the Arizona monsoon Cu ranged in size from Cu humilis to cumulonimbus. Almost all high plains Cu and most Arizona monsoon Cu contained ice. There was a range of vertical velocities in the sampled Cu, implying that all stages in the life cycle of Cu towers were sampled. Most clouds were rising, but a significant fraction of the Cu was sampled in their decaying phase with mainly sinking motion at flight level. The (orographic)

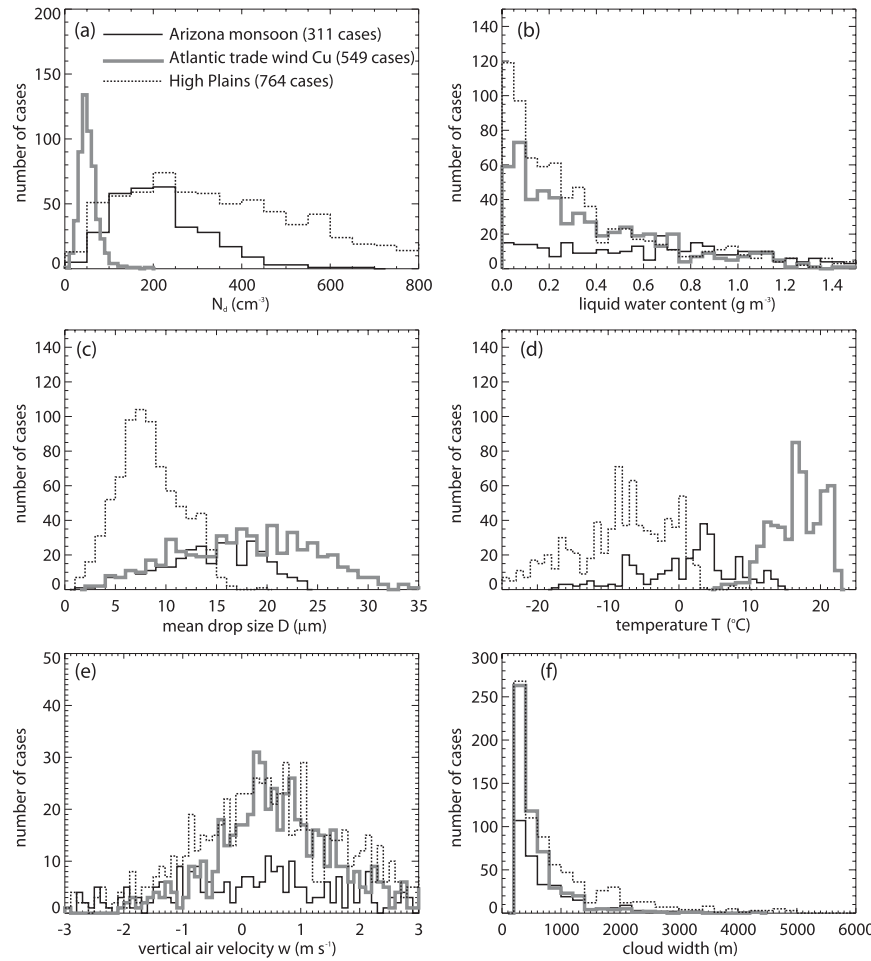


FIG. 3. Histograms of the mean properties of the cumuli in three environments. (a) The total number of Cu samples in each environment.

Arizona monsoon Cu tended to have stronger updrafts and downdrafts than the Atlantic trade wind Cu (Fig. 3e). This is consistent with the higher convective available potential energy in MGAUS soundings released during the WKA flights in CuPIDO-06 (806 J kg^{-1} on average) than in RICO-04 (228 J kg^{-1} on average). Some 92% of the penetrated Cu were less than 2000 m wide, yet some Cu were as wide as 6 km (Fig. 3f).

In short, the dataset of 1624 Cu penetrations represents mostly Cu mediocris in a range of dimensions, Cu life cycle stages, and ambient conditions.

b. Horizontal structure of cloud and dynamical variables

1) CLOUD MICROPHYSICAL VARIABLES

Histograms of N_d and LWC are shown in Fig. 4a and Fig. 5a at all x^* distance bins. The frequency field is shaded. We refer to these displays as frequency by dis-

tance, in analogy with the frequency by altitude displays introduced by Yuter and Houze (1995). Because there is a large range in mean values of mainly N_d and also LWC (Figs. 3a,b), these variables are normalized by the mean value \bar{N}_d in $-1.0 < x^* < 0.0$ (i.e., $N_d^* = N_d / \bar{N}_d$) and by the adiabatic LWC LWC_a (i.e., $LWC^* = LWC / LWC_a$) for each individual Cu penetration in Fig. 4a and Fig. 5a, respectively. We refer to LWC^* as the adiabatic fraction—that is, the ratio of the local LWC over the adiabatic LWC of the sampled cloud. The adiabatic LWC is computed from the LCL pressure and temperature and the flight level following Albrecht et al. (1990). Both N_d^* and LWC^* vary significantly at all ranges from the cloud center. The normalization of N_d and LWC brings out the remarkable along-track variability. Close to the cloud edge, both variables approach zero. The mean values (shown as a bold line in Figs. 4a, 5a) indicate that both N_d^* and LWC^* decrease very slightly from the cloud center to $x^* = -0.15$ and that they plummet from there to the cloud

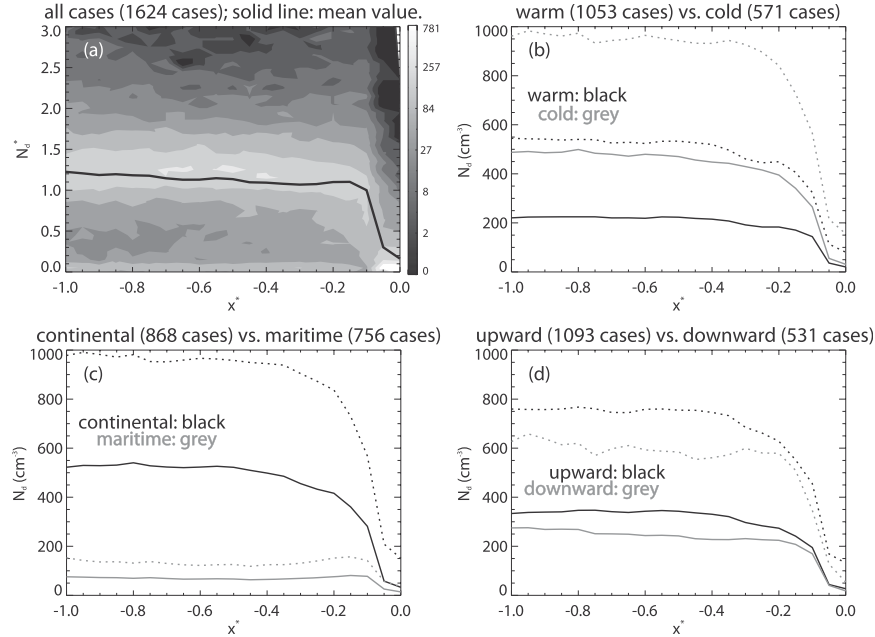


FIG. 4. Variation of cloud droplet concentration N_d with normalized distance from the cloud center ($x^* = -1$) to the cloud edge ($x^* = 0$). (a) Frequency by distance display of the normalized cloud droplet concentration N_d^* . The black line indicates the mean. The other plots show the mean variation of N_d with distance for (b) warm and cold cloud penetrations (the mean temperature threshold is -5°C), (c) maritime and continental cloud penetrations (the mean N_d threshold is 150 cm^{-3}), and (d) rising and sinking motion, on average, at flight level. In (b)–(d) and in later figures, the dotted lines indicate the mean plus one std dev. The number of cases is listed on top of each plot.

edge. The slow decrease of both variables, mainly in $-0.50 < x^* < -0.10$, appears to occur in continental clouds only (Figs. 4c, 5c) and mainly in updrafts—that is, in younger clouds (Figs. 4d, 5d). The Atlantic trade wind Cu tend to have weaker updrafts (Fig. 3e) and a lower buoyancy flux (see below), and thus less turbulence near the cloud edge. This may help to explain the lack of a decrease in N_d^* and LWC* from the cloud center to $x^* = -0.10$.

The most significant finding from Fig. 4 and Fig. 5 is the rapid decrease in N_d^* and LWC* near the cloud edge and mainly in $-0.10 < x^* < -0.05$, suggesting that significant lateral entrainment is limited to this depth, which corresponds to a shell with a thickness of 10% of the cloud radius. The same applies to the mean droplet diameter, which otherwise shows far less variability in individual Cu penetrations than N_d^* and LWC* (not shown). The remarkably uniform mean droplet diameter in the cloud (within $x^* \leq -0.10$) is consistent with other studies (e.g., Paluch and Knight 1984).

The Cu core appears to be diluted more by vertical entrainment (including cloud-scale eddies such as a cloud-top toroidal circulation) than by lateral entrainment, since the cloud droplet characteristics are fairly uniform in the Cu core (Figs. 4, 5) and the most common adiabatic

fraction LWC* is quite small, below 5% (Fig. 5a). Notice that LWC* may have been underestimated in some cases, as some liquid water may have been lost through precipitation and some water may have been in the ice phase. We examine the differences between more and less adiabatic cases in Fig. 6 using a threshold mean adiabatic fraction of 15%. The more adiabatic cases tend to have stronger updrafts and more numerous and larger droplets, because they probably are younger Cu clouds. These clouds also tend to carry more excess heat relative to their environment, compared to less adiabatic, older clouds (Fig. 6e). Therefore, one would expect the more adiabatic cases to be more buoyant as well but because of their larger LWC (Fig. 6b) the more adiabatic Cu samples tend to have weaker positive buoyancy in-cloud than the less adiabatic Cu samples (Fig. 6f). Buoyancy is discussed further in section 3. Both young and old clouds are characterized by a narrow margin of cloud microphysical change just inside the cloud edge.

2) KINEMATIC VARIABLES

The vertical velocity (w) composites (Fig. 7a) yield two findings that are not surprising: 1) w varies more in-cloud than in the clear-air shell as the standard deviation

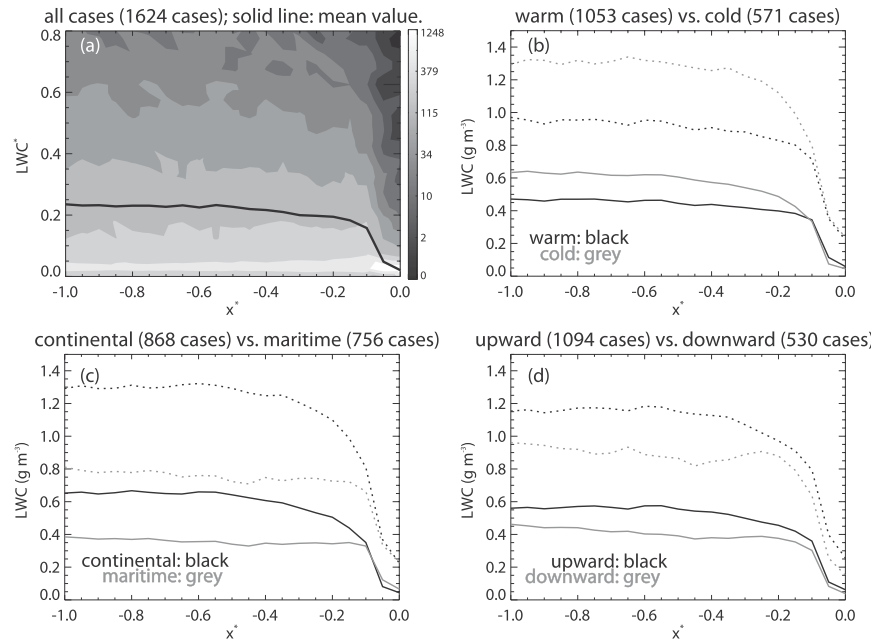


FIG. 5. Same as Fig. 4, but for (a), where LWC is normalized by the cloud's adiabatic LWC.

of w at $x^* = -1.0$ is about twice that at $x^* = +1.0$; and 2) updrafts (downdrafts) prevail in (out of) cloud, although nearly one-third of the Cu were sampled in a late stage with downdrafts prevailing across the cloud (Fig. 7d). There are two other findings that are more surprising.

First, the idea that vertical motion in the clear-air shell simply “compensates” the Cu vertical motion, often does not apply. Only a small fraction of Cu are characterized by substantial rising motion in-cloud and substantial compensating sinking motion around the cloud (the upper left quadrant in Fig. 8). According to Fig. 8, a stronger Cu updraft (downdraft) does not imply a stronger clear-air shell downdraft (updraft). There is no significant correlation between mean w (in cloud) and mean w (clear air). Most points in Fig. 8 do fall in the upper left quadrant (cloud updraft, shell downdraft), as expected, but we further expected most of the points in Fig. 8 to lie in an ellipse centered in the upper left quadrant with the long axis pointing up (because in-cloud drafts are larger than the clear-air shell drafts, Fig. 7) and tilted from the upper left to the lower right. Instead, the distribution in Fig. 8 stretches from the lower left to the upper right. This suggests that the clear-air shell ($0.0 < x^* < +1.0$) tends to be dragged along somewhat with the cumulus draft, especially in the Cu decaying phase. Thus compensating vertical motion must occur at some time lag and/or outside the clear-air shell ($x^* > +1.0$).

Second, the clear-air shell does not respond uniformly. Air tends to sink more rapidly in the cloud margin ($-0.2 < x^* < +0.2$) than in the surrounding clear air, which is

consistent with Jonker et al. (2008). This tendency even applies in old clouds that are less adiabatic (Fig. 6d) and subsiding (Fig. 7d). The variation in vertical motion from Cu center to Cu edge is consistent with a toroidal ring circulation in Cu towers (Zhao and Austin 2005b; Damiani et al. 2006) but also with other idealized flow patterns for thermals.

The vertical mass transport in the cloud and its immediate environment can be estimated in two ways. First, if we assume radial symmetry around the cloud center, the cumulative vertical flux M (kg s^{-1}) within a radius (r) from the cloud center can be computed as $\dot{M} = \int_0^R \rho w 2\pi r dr$, where ρ is air density and r radius. This also assumes that the center point along the track through a penetrated Cu corresponds with the cloud center. This does not generally apply (although the WKA flight strategy was to target the visual cloud center upon approach) but nevertheless the method is still meaningful. Conversely, if we assume that the penetrated Cu is part of a band stretching in the cross-track dimension, then the cumulative vertical mass flux would be $\dot{M} = L \int_0^X \rho w dx$, where L is the length in the third (along-band) dimension, and X is the distance from the cloud center.

The cumulative vertical mass transport per unit area is shown in Fig. 9a under these two different assumptions. The more plausible radial symmetry assumption yields net upward mass transport within the 1624 clouds sampled, but the ambient downward flux exceeds the in-cloud upward flux starting at $x^* = +0.40$ with a substantial net downward flux at $x^* = +1.0$. One would expect the

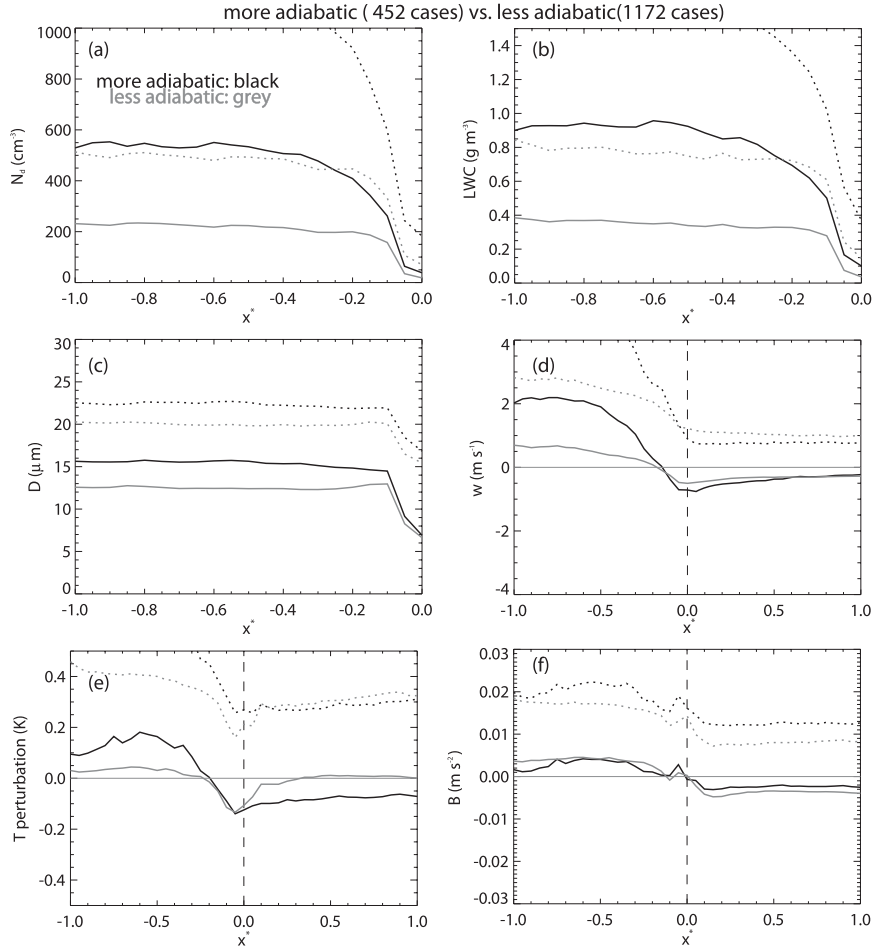


FIG. 6. Variation of (a) N_d , (b) LWC, (c) mean drop diameter D , (d) w , (e) T , and (f) buoyancy with normalized distance x^* for more adiabatic and less adiabatic cases. The mean value (solid line) and the average plus one std dev (dashed line) are shown. The threshold adiabatic fraction (the ratio of the mean LWC in-cloud over the adiabatic LWC of that cloud) is 15%.

integrated mass flux to be near zero at $x^* = +1.0$ or even slightly positive if some of the compensating subsidence occurs at a greater range from the cloud. The assumption of radial symmetry may offer some explanation. This assumption maximizes the area of the clear-air shell. In reality, another cloud may be present within $x^* = +1.0$ in an off-track direction, adding subsidence, or the cloud may be elongated in the off-track dimension. If the off-track cloud length is infinite (i.e., the “cloud band” assumption in Fig. 9a), then the cumulative vertical mass flux remains positive out to $x^* = +1.0$. The apparent net downward mass flux over the Cu clear-air shell ensemble (Fig. 9a) may be due, in part, to biased sampling, in two regards. First, some 33% of the sampled Cu experience subsidence on average (Fig. 7d) and these Cu may be overrepresented. In aircraft-based sampling such bias naturally results from the time lag

between spotting a Cu target and penetrating it. This time lag is short, but not insignificant compared to the typical lifespan of a Cu tower. And second, most Cu penetrations were in the upper cloud half (see below) and net downward mass flux over an area encompassing the cloud and the clear-air shell is found in upper-level penetrations only, not in penetrations closer to the cloud base (Fig. 9b). This is consistent with the LES study by Zhao and Austin (2005a).

A perturbation “radial” velocity (v_{rad}) can be computed as the departure from the average along-track wind between $-1.0 < x^* < 1.0$. We call v_{rad} a radial wind because it blows across the cloud edge, but it can be thought of as the across-band wind if the Cu is considered to be part of a line of convection. Two observations stand out in the mean pattern of v_{rad} (Fig. 10). First, the radial velocity increases within the cloud, out to about

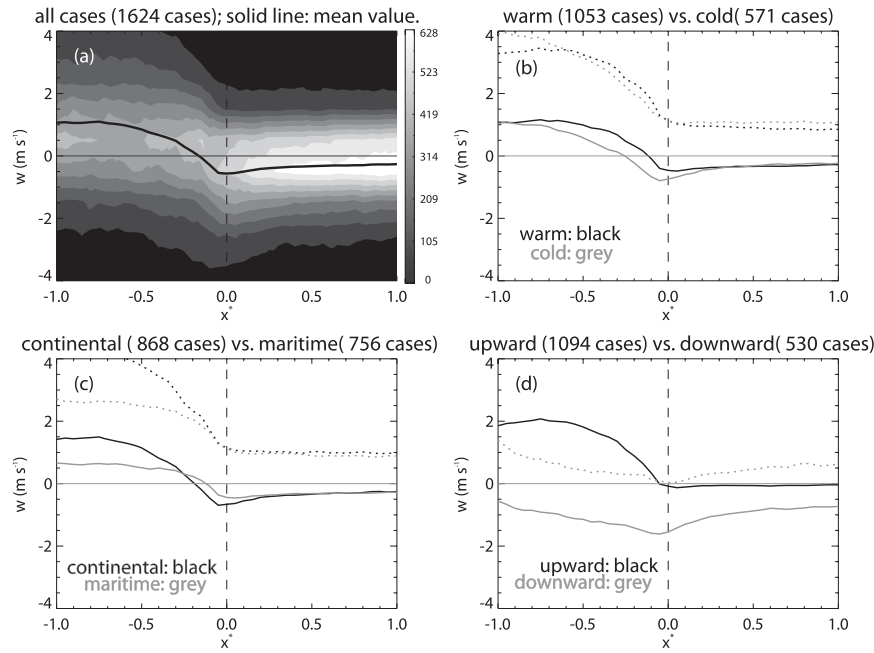


FIG. 7. Variation of w with normalized distance from the cloud center ($x^* = -1$) into the clear air, over a distance matching that in-cloud ($x^* = +1$). (a) Frequency by distance display of w . Note the linear scale of frequencies. The black line indicates the mean. The other plots show the mean variation of w with distance for (b) warm and cold cloud penetrations, (c) maritime and continental cloud penetrations, and (d) rising and sinking air, on average, at flight level. The thresholds are the same as in Fig. 4. The number of cases is listed on top of each plot.

$x^* = -0.2$, especially in the more vigorous Arizona monsoon Cu (Fig. 10a). This suggests horizontal divergence (div), which is calculated in Fig. 10c using the same two basic assumptions for \dot{M} —that is, radial symmetry (div = $1/r\partial r v_{\text{rad}}/\partial r$) and banded clouds (div = $\partial v_{\text{rad}}/\partial x$). The prevailing divergent flow within the Cu core suggests that most of the sampled Cu were close to the equilibrium level on a thermodynamic diagram (i.e., the cloud top). The horizontal divergence implies decreasing updraft strength, assuming incompressible air mass continuity. This is addressed further in section 3.

A second observation in Fig. 10 brings us back to the localized subsidence at the cloud margin (Fig. 7a)—that is, the radial velocity decreases rapidly across the cloud margin (roughly $-0.2 < x^* < +0.2$; Fig. 10a). This implies convergent flow within the cloud margin (Fig. 10c), especially in the upper cloud regions (Fig. 10d). Convergence implies that the cloud margin subsidence intensifies downward and this suggests downward acceleration. Such downward acceleration may be caused by “compensating” forcing (i.e., the pressure perturbation acceleration induced by the Cu buoyant core). This forcing conceptually operates on a larger scale outside the cloud [e.g., Fig. 8.1 in Houze (1993)]. The downward acceleration may also be caused by evaporative cooling, both in entraining and in detrainning eddies. This interpretation

is consistent with the decrease in LWC near the cloud edge (Fig. 5) and with the negative temperature anomaly around the cloud edge (Fig. 11). It is also consistent with the fact that the LWC depletion (Fig. 5c), the cloud

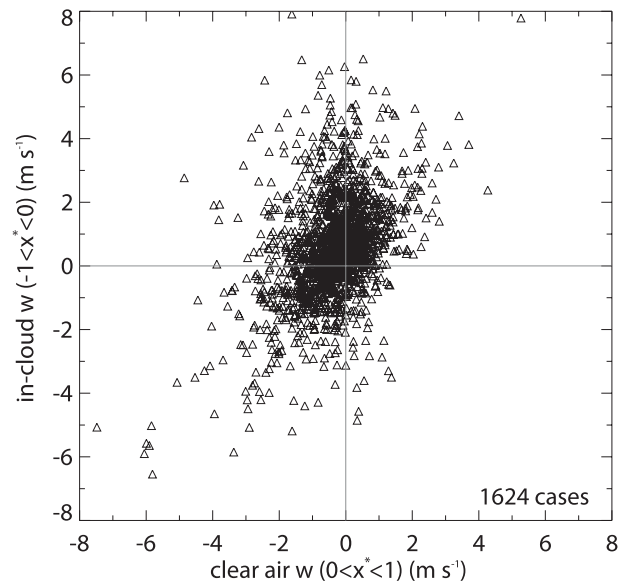


FIG. 8. Scatterplot of in-cloud vs out of the cloud mean w .

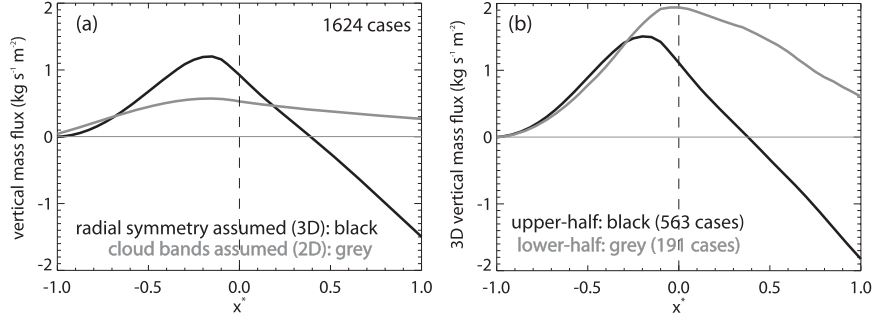


FIG. 9. The cumulative vertical mass flux per unit area integrated from the cloud center, (a) derived from the mean w shown in Fig. 7a for the 2D and 3D assumptions, and (b) for flight levels in the upper half of the cloud and those closer to cloud base, both using the 3D assumption.

margin downdraft (Fig. 7c), and the cool anomaly (Fig. 11c) are all more pronounced in continental clouds (with lower mean ambient relative humidity) than maritime clouds in a more humid environment. Finally, it is consistent with the LI-COR 6060 water vapor increase toward the cloud edge, a result of detrainment (entrance trace in Fig. 2). Notice that the entrance trace in Fig. 2 is unbiased (section 2). This increase may be weak, but at least the near-cloud clear-air shell does not have the water vapor deficit that would be expected of simple compensating subsidence [see Fig. 6 in Rodts et al. (2003)].

3) DYNAMIC VARIABLES

We now examine whether the local cloud margin subsidence is buoyancy driven. Buoyancy is not only derived from temperature and humidity anomalies but is also affected by hydrometeor loading. We computed buoyancy B (m s^{-2}) including all terms in the equation [e.g., Eq. (2.51) in Houze (1993)], except the pressure perturbation term, which is ignored because the static air pressure is not known with enough precision:

$$B = g \left[\frac{\theta'}{\theta_o} + 0.61q'_v - q_H \right]. \quad (1)$$

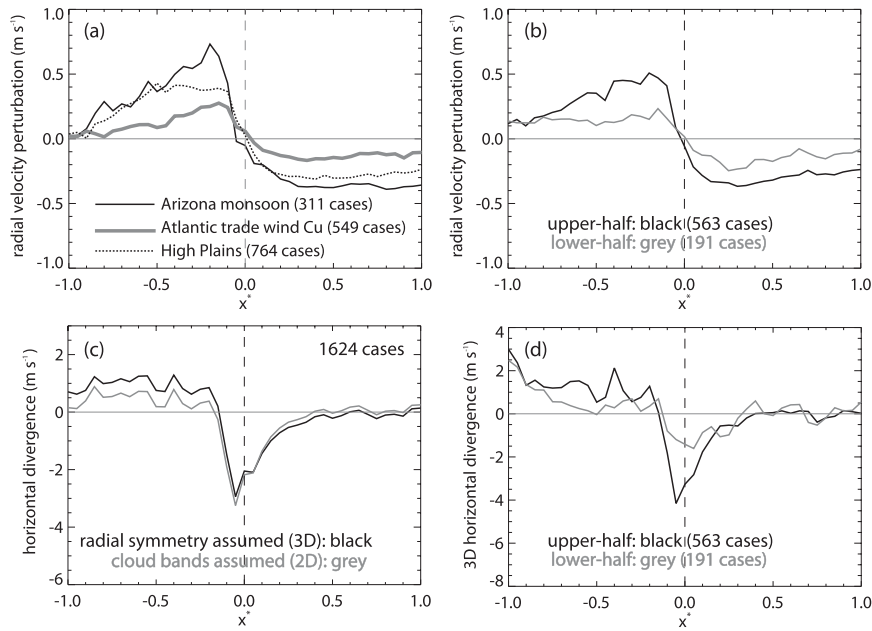
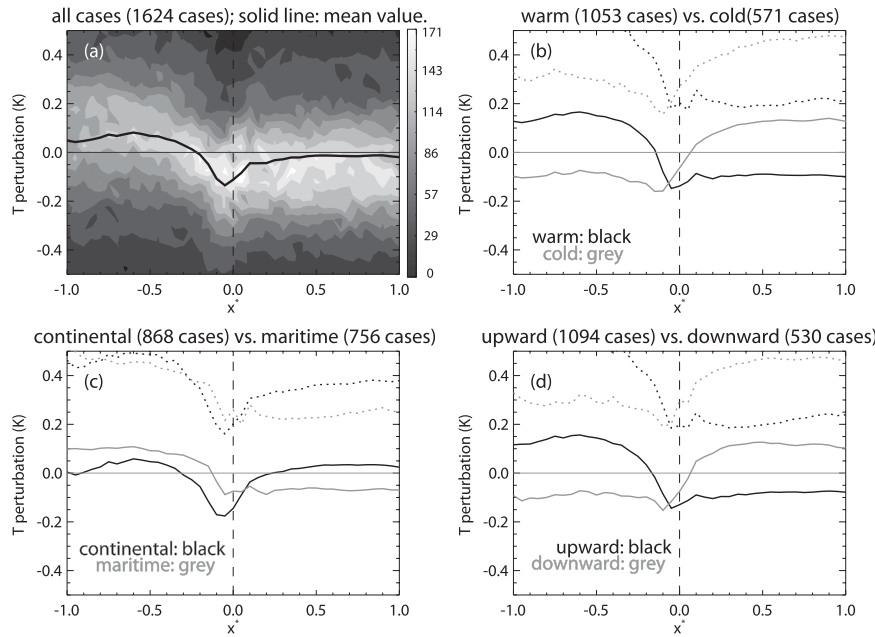


FIG. 10. (top) Variation of the mean horizontal “radial” velocity from the cloud center to the clear-air shell. This velocity is defined to be positive for outbound flow, away from the cloud center. It is a perturbation value, i.e., the mean between $-1 < x^* < 1$, that is removed for each penetration. The contrasts of the (a) three environments and (b) the flight levels in the upper half of the cloud against those in the lower half. The horizontal divergence resulting from the mean radial velocity is shown for (c) all cases and (d) upper-level vs lower-level penetrations.

FIG. 11. Same as Fig. 7, but for T .

Here θ is the potential temperature (K), q_v is the mixing ratio of water vapor (kg kg^{-1}), and q_H is the mixing ratio of liquid and/or frozen water (kg kg^{-1}). The parameters with a prime (' \prime ') represent the deviation from the reference values, while the ones with subscript "o" denote the reference states. Ideally, the reference state would be represented by the far-field environment surrounding a cumulus cloud. Because other Cu were often present beyond $x^* = 1.0$, we compute the reference temperature as the average value in $-1.0 < x^* < 1.0$. Because of the very slow response of the chilled mirror dewpoint sensor, the reference water vapor mixing ratio q_v is computed over 500 m before the aircraft entered the cloud. The in-cloud value of q_v is assumed to be the saturated value computed from local temperature and pressure, whereas the measurement from the chilled mirror dewpoint sensor is used for q_v outside of the cloud. The hydrometeor loading term q_H includes ice water, although in cold clouds ($<-5^\circ\text{C}$) the ice water content was found to be an order of magnitude smaller than the LWC, on average, in the sample. As previously defined, the mean buoyancy in $-1.0 < x^* < 1.0$ is not zero; therefore, as a final step we removed the mean buoyancy for each transect. The sign of B (positive or negative) is less meaningful than the value of B at some point relative to its value in surrounding areas (Doswell and Markowski 2004). The horizontal gradient of B is dynamically meaningful as it drives horizontal vorticity—that is, the toroidal circulation around the cloud edge, $D\eta/Dt = \partial B/\partial x$, where D/Dt is the total derivative, and $\eta = \partial v_{\text{rad}}/\partial z - \partial w/\partial x$ the horizontal vorticity.

Buoyancy patterns in and around Cu are shown in Fig. 12. The cool anomaly peaks at $x^* = -0.05$ (Fig. 11a), but the LWC is much lower than deeper in-cloud (Fig. 5a). Thus, the negative temperature anomaly and the low hydrometeor loading largely compensate, resulting in a weak local buoyancy maximum at $x^* = -0.05$ (Fig. 12a). The clear-air shell is negatively buoyant compared to the cloud, with a local minimum at $x^* = +0.15$ (Fig. 12a). The buoyancy difference between clear air, cloud, and the local B minimum close to the cloud edge is 10%–20% larger if the reference value of q_v (rather than the local value) is used outside the cloud. This is because of the slow response of the chilled mirror dewpoint sensor, which overestimates the humidity where the aircraft exits the cloud. Buoyancy is overestimated where humidity is overestimated [Eq. (1)].

Sinking cumuli tend to be slightly negatively buoyant relative to their immediate environment (Fig. 12d). On average, the buoyancy flux¹ is positive in-cloud (where

¹ Notice that the buoyancy flux is computed using perturbation quantities over the distance $-1.0 < x^* < 1.0$ only and the hydrometeor loading term is retained in the expression for buoyancy. In noncloudy environments, the buoyancy flux is proportional to $\bar{w}'\bar{\theta}'_v$, where θ_v is the virtual potential temperature and the overbar indicates a Reynolds average. The Reynolds average in the calculation of buoyancy flux and TKE applies to all cases in the composite, unlike the common method in which averages in time or space are computed. Thus, the Reynolds average is computed at any location (x^*) as the average of the products of two perturbation quantities (departures from the mean value between $-1.0 < x^* < 1.0$).

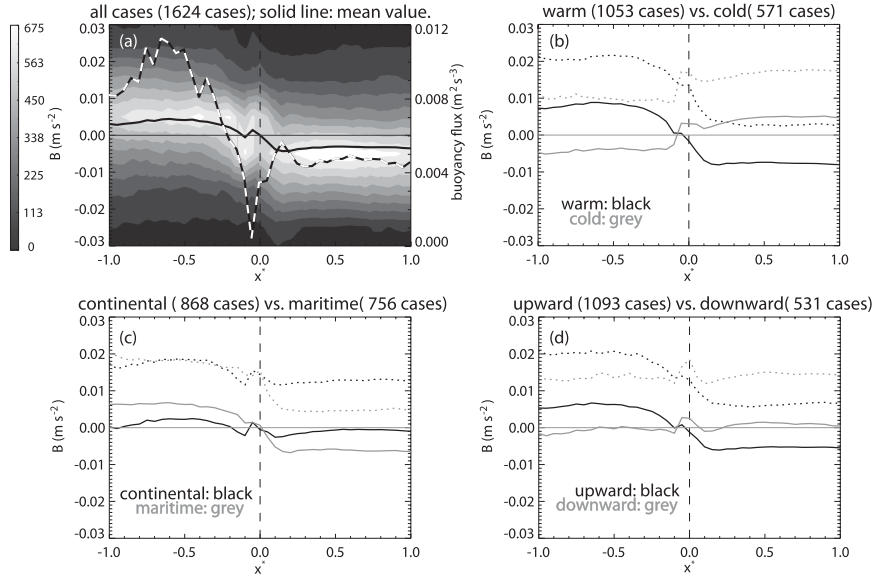


FIG. 12. Same as Fig. 7, but for B . Also shown is (a) the vertical buoyancy flux (black and white dashed line).

positive buoyancy and updrafts dominate), near-zero in the cloud margin (where buoyancy is small), and more positive again in the clear-air shell (where negative buoyancy and downdrafts dominate), but there the buoyancy flux is only about half as large as in-cloud (Fig. 12a).

Thus turbulent kinetic energy (TKE) is generated mainly in-cloud, but also outside of the cloud (Fig. 13). TKE is generated not only by buoyancy flux, but also by the shear in vertical velocity between the cloud core updraft and the cloud margin subsidence [e.g., Eq. (5.2.3) in Stull (1988)]. We computed TKE as the Reynolds average of the perturbations from the mean wind in three dimensions (u' , v' , w') in the region $-1.0 < x^* < +1.0$:

$$\text{TKE} = 0.5(\overline{u'^2} + \overline{v'^2} + \overline{w'^2}). \quad (2)$$

Typical TKE values are about 3 times larger in the middle of the Cu than in the clear-air shell and they do not reach a minimum near the cloud edge. They are larger in the more vigorous Arizona monsoon Cu than in the Atlantic trade wind Cu. In watching a towering Cu develop, we may assume that turbulence is contained and generated only within the cloud. Clearly, turbulence is present and continuously generated also near the cloud edge and even in the clear-air shell.

Some of the results shown can only be explained by the flight strategies in the various field campaigns. For instance, continental Cu (i.e., most high plains Cu and Arizona monsoon Cu) were generally sampled near the cloud top, often near a stable layer (i.e., the equilibrium level), where most clouds still had much rising motion

(Fig. 7c) but little buoyancy (Fig. 12c). A key objective in these campaigns was to capture Cu convection with the dual-Doppler WCR antennas below the aircraft. Aircraft penetrations through the upper half of the cloud show stronger divergent flow within the Cu core (Figs. 10b,d), consistent with a flight level near the equilibrium level. All the “cold” ($<-5^\circ\text{C}$) Cu penetrations are high plains Cu or Arizona monsoon Cu, and this may explain the remarkable negative buoyancy of “cold” clouds (Fig. 12b), because apparently some of the cold Cu towers were overshooting (Fig. 11b). Clearly, more can be learned if we can stratify the horizontal structure statistics by the cloud-relative flight level.

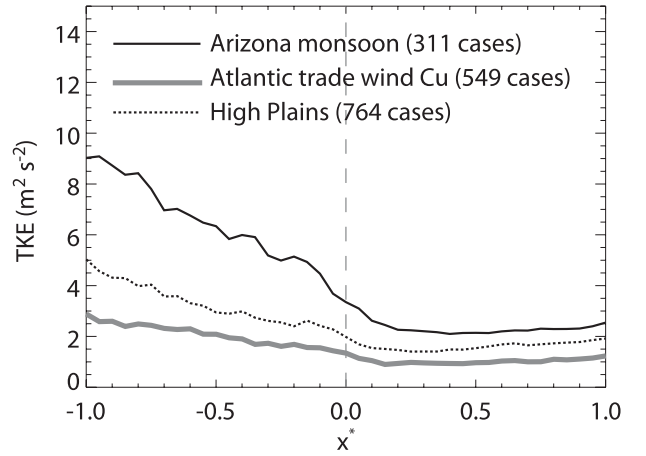


FIG. 13. Mean TKE for all Cu for the three environments.

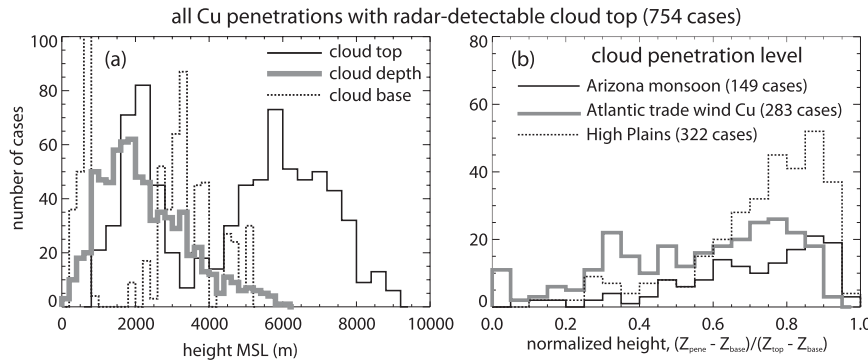


FIG. 14. Histograms of (a) cloud vertical dimensions and (b) flight level relative to the cloud vertical dimensions. Here, Z_{pene} , Z_{base} , and Z_{top} are the penetration level, the cloud base, and the cloud top, respectively.

c. Cloud depth and flight level

The subset of Cu, with cloud-top and cloud-base information (section 2), displays bimodal cloud-base and cloud-top distributions, with Atlantic trade wind Cu, all with a cloud base below 1000 m MSL, and a cloud top below the freezing level, whereas other Cu have a much higher cloud base and generally peak above the freezing level (Fig. 14a). Yet, the cloud depth distribution has a single peak, because just over half of the clouds in the sample are at least 2000 m deep and some are as deep as 6000 m. The Atlantic trade wind Cu are the most shallow on average, and the high plains Cu the deepest. Nearly half (43%) of all cloud penetrations were in the upper quarter of the cloud—that is, above a normalized height of 0.75 (Fig. 14b). Only a quarter of all cloud penetrations were in the lower half of the cloud. The cloud penetration level distribution was most uniform for the Atlantic trade wind Cu and most biased toward cloud tops for the high plains Cu.

We used this Cu depth information to contrast “deep” Cu against “shallow” Cu, with a threshold depth corresponding with a 50–50 split in each of the three environments. Deep Cu tend to have more liquid water and a weaker warm anomaly, and therefore they are less buoyant than shallow Cu but the updraft strength and vertical buoyancy flux are about the same (not shown). Larger differences emerge from a contrast between lower and upper cloud-level penetrations (Fig. 15). The upper-cloud penetrations encounter much more liquid water, as can be expected from moist-adiabatic ascent. The horizontal variation of LWC near the cloud edge (discussed in section 3) is unaffected by flight level. The upper-cloud penetrations include both strongly buoyant cores and negatively buoyant (overshooting) towers and both strong updrafts and strong downdrafts (note the large standard deviations for upper-half penetrations in Figs. 15c,d,e). The lower-cloud penetrations see much

less variation in buoyancy and vertical velocity. Both buoyant updrafts and negatively buoyant collapsing towers contribute to a large buoyancy flux in the upper regions of the cloud and the surrounding clear-air shell (Fig. 15f) and as a result TKE generation by the buoyancy flux is much larger there (not shown).

Three observations give evidence for the concept of a cloud-top toroidal ring, which contains the least diluted air (Blyth 1993; Carpenter et al. 1998; Zhao and Austin 2005b; Damiani et al. 2006). The first two regard the kinematics, the last relates to the dynamics. First, at upper levels in a Cu the updraft peaks near the center and becomes negative in the cloud margin (implying much horizontal vorticity), while at lower levels the updraft is weaker and more uniform within the cloud (Fig. 15d). Near the cloud top the toroidal ring appears to merge with a broader circulation that includes subsidence in the clear-air shell. Second, at upper levels (more so than at lower levels) the horizontal flow is divergent in the Cu core and convergent in the cloud margin (Fig. 10d). Third, the upper-cloud data suggest that the warmest and most buoyant part of the cloud is not the center (as it is in the lower half of the cloud), but rather near $x^* = -0.5$ (Figs. 15c,e).

4. Horizontal cloud structure in physical space

We found that liquid water becomes depleted near the cloud edge and a temperature deficit and subsidence occur in a cloud margin roughly $-0.2 < x^* < 0.2$ wide. But there is no reason to expect the cloud margin width to scale with cloud diameter (Jonker et al. 2008). To discover the typical actual width of the cloud margin, we map the composites shown earlier in physical rather than normalized space (Fig. 16). The drawback of this approach is that the sample size decreases rapidly with distance from the cloud edge (past the minimum half-cloud width of 100 m), but statistical significance can be

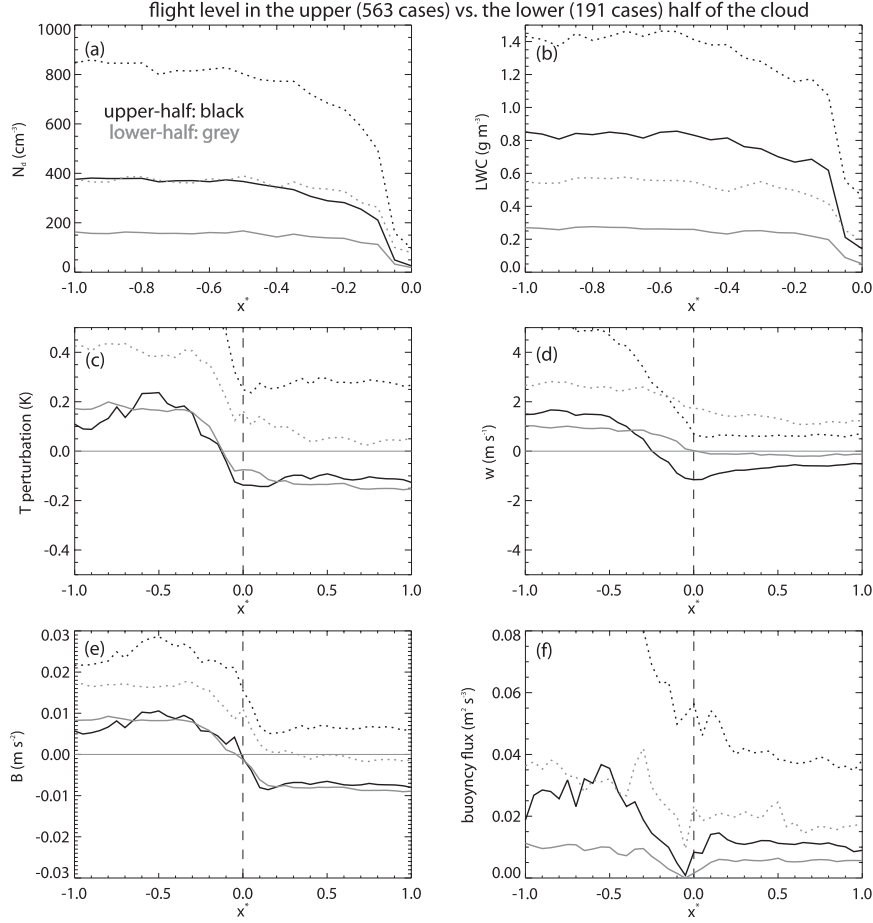


FIG. 15. Mean variation of (a) N_d , (b) LWC, (c) T , (d) w , (e) B , and (f) buoyancy flux with normalized distance x^* for upper-level and lower-level flight levels.

judged by considering this sample size, shown as a dotted line in Fig. 16.

Both N_d (Fig. 16a) and LWC (Fig. 16b) decrease steadily from about $x = -700$ m to the cloud edge, thus the typical lateral entrainment depth of eddies (before they mix at fine scales with cloud air) is less than 700 m. The TKE is maximum in-cloud and decays steadily toward the cloud edge starting at roughly 700 m (Fig. 16f). The mean updraft strength (Fig. 16d) weakens from about the same distance toward the cloud edge, where downdrafts prevail. This is consistent with the results in normalized space (Fig. 7), with the one difference being that downdrafts only prevail partly outside of the cloud ($0 < x < 700$ m) and then updrafts dominate ($x > 700$ m, where the sample size becomes very small), whereas downdrafts prevail throughout the clear-air shell in normalized space. More important is the observation that downdrafts prevail near the cloud edge, between about 70 m in-cloud and a few 100 m outside of cloud, peaking at about -0.7 m s^{-1} , precisely at the cloud edge. The width and magnitude of

this downdraft is roughly consistent with measurements documented in Jonker et al. (2008) and Heus et al. (2009).

A dynamical relationship is suggested by the matching asymmetric shape of subsidence (Fig. 16d), cold anomaly (Fig. 16c), and buoyancy (Fig. 16e) within roughly $-200 \text{ m} < x < 200 \text{ m}$. These values decline rapidly in $-100 \text{ m} < x < 0$ and recover more slowly in the clear-air shell. The region of $-100 \text{ m} < x < 100 \text{ m}$ is also the region of strongest horizontal convergence, which peaks precisely at the cloud edge (not shown). Convergence implies local downward acceleration of the downdraft ($\partial w / \partial z > 0$), thus negative advection ($w \partial w / \partial z < 0$) and downward forcing follow the parcel subsiding in the cloud margin (total derivative $Dw / Dt < 0$). Downward forcing in the region $-200 \text{ m} < x < 200 \text{ m}$ is consistent with a cold anomaly (Fig. 16c) and negative buoyancy (Fig. 16e). Negative buoyancy is present only on the clear-air side ($0 < x < 200 \text{ m}$) and there is a positive B spike near the cloud edge (at $x = -10 \text{ m}$), because of the sudden disappearance of liquid water (Fig. 16b).

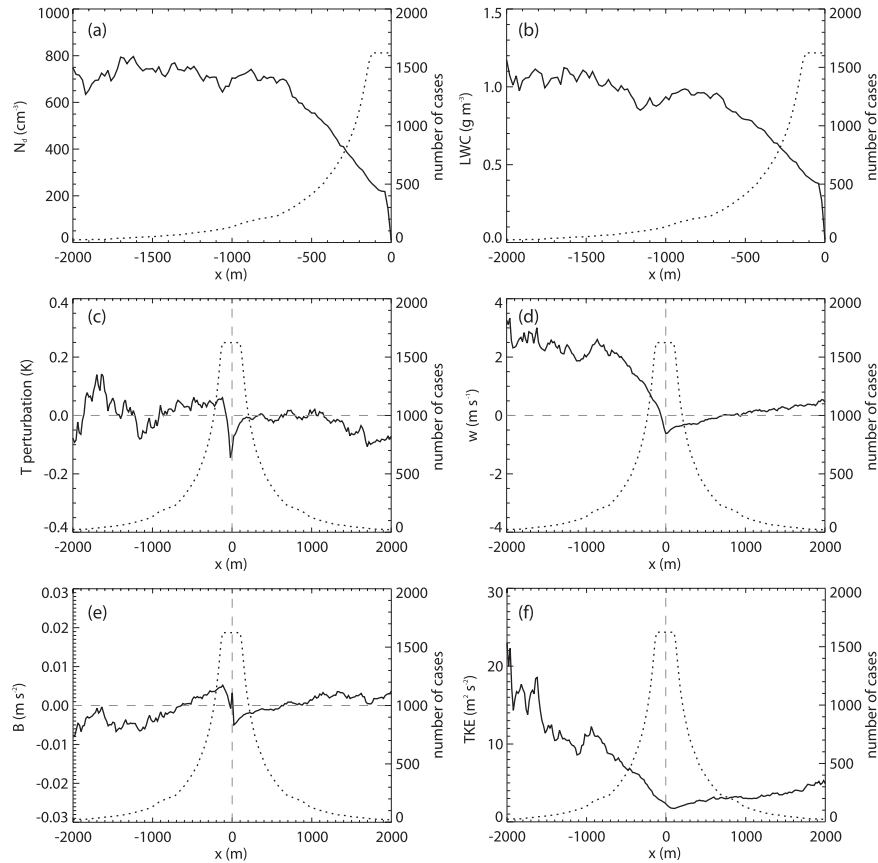


FIG. 16. Mean variation of (a) N_d , (b) LWC, (c) T , (d) w , (e) B , and (f) TKE with physical distance x . The dotted line shows the number of penetrations (frequency) as the function of x . Notice that this dotted line is flat for $|x| < 100$, since the minimum cloud width in the sample is 200 m. The cloud edge is at $x = 0$ and the cloudy region corresponds with $x < 0$.

The widest clouds sampled tend not to harbor a positive temperature anomaly and with significant water loading their core buoyancy tends to be negative. This is interpreted as a sampling bias toward older clouds spreading out near the equilibrium level. In summary, the Cu cloud margin extends ~ 200 m from the cloud edge and the effect of laterally entraining eddies is apparent to a depth of ~ 700 m in-cloud.

5. Discussion: Cloud margin subsidence and evaporative cooling

Our sample of 1624 Cu penetrations is not unbiased, in particular in terms of flight level and cloud age, but it is the most detailed database to date for the study of the characteristic horizontal structure of Cu. The observed presence of a sinking motion in the cloud margin confirms previous studies. The cloud margin—that is, the transition region in which lateral entrainment is significant—roughly corresponds with $-0.2 < x^* < +0.2$, and with $-200 \text{ m} < x < 200 \text{ m}$. The sinking air current appears to

be anomalously cool and appears to accelerate downward. Except for a positive spike just inside the cloud edge, the cloud margin air is negatively buoyant compared to the surrounding air in the Cu core and the clear-air shell. This observation suggests that entraining eddies, driven by the convective circulation mix environmental air, are more effective in the margin of cumulus clouds than deep into the cloud core. Turbulent mixing tends to deform volumes of entrained air into thinner, smaller filaments until the Kolmogorov scale is reached. Much of this mixing appears to be accomplished before the Cu core is reached.

As further evidence for the hypothesis that evaporative cooling in the cloud margin drives subsidence, we divide the entire sample in two classes depending on ambient humidity (Fig. 17). Evaporative cooling is proportional to the vapor pressure deficit $e - e_{\text{sat}}(T)$, where e is the ambient vapor pressure and $e_{\text{sat}}(T)$ the saturation vapor pressure with respect to water at temperature T in-cloud. For each penetration, $e_{\text{sat}}(T)$ was calculated in-cloud only ($-1.0 < x^* < 1.0$) and e was derived from

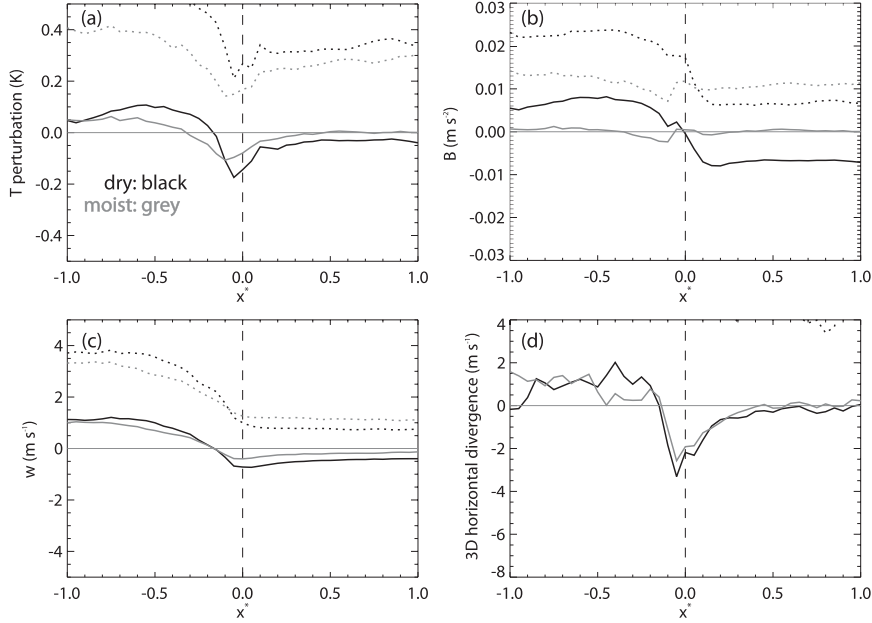


FIG. 17. Mean variation of (a) T , (b) B , (c) w , and (d) divergence (assuming radial symmetry) with normalized distance for dry vs moist environments.

$e = e_{\text{sat}}(T_d)$, where T_d is the average chilled mirror dewpoint in the 500 m just up-track of the cloud. The threshold vapor pressure deficit that divides the population in two equal groups is 1.57 hPa.

Clearly, in a dry environment the cool anomaly, negative buoyancy relative to the Cu core subsidence and convergence (downward acceleration) in the cloud margin is at least slightly stronger than in a moist environment (Fig. 17). The Cu cases in dry environments are far more buoyant than those in moist environments primarily because they contain less liquid water. Closer inspection shows that many penetrations in the moist environment group occurred near the cloud top where significant detrainment occurred. In any event, the comparison in Fig. 17 supports the hypothesis that cloud margin subsidence is not “compensating” (a cloud-scale mass continuity response) but rather is forced by local negative buoyancy as a result of evaporative cooling in entraining and detaining eddies. This finding is generally consistent with findings in Rodts et al. (2003), who studied shallow Cu over Florida in summer and with findings in Heus et al. (2009). Gerber et al. (2008), examining mixing properties in RICO cumuli in a composite sense, note that the near-cloud environmental air differs significantly from the distant environmental air. Grabowski (1993) uses theoretical arguments and high-resolution model simulations to demonstrate cumulus edge buoyancy reversal caused by entrainment of dry environmental air. As entraining eddies, associated with baroclinically induced cloud interface instability, trans-

fer their energy to smaller scales turbulence effectively and rapidly mixes dry and cloudy air, resulting in local buoyancy reversal (Grabowski and Clark 1993). Finally, Jonker et al. (2008) use LES to confirm that much of the compensating downward mass transport around Cu occurs in a thin shell just outside the cloud edge.

This conclusion implies that the clear-air subsidence in a field of Cu clouds tends to be more humid than soundings suggest, since clear-air soundings (the ones not contaminated by cloud) are typically collected farther from the clouds. Therefore, the use of sounding data may underestimate the downward moisture transfer in the environment surrounding Cu and overestimate the mean net upward moisture transfer by a field of Cu (e.g., Lin and Johnson 1996; Frank et al. 1996). This may have implications for cumulus parameterizations in NWP and climate models.

6. Conclusions

This paper analyzed the composite horizontal structure of shallow to moderately deep cumulus clouds from the cloud center across the cloud edge into the ambient clear air. The cumuli were sampled by aircraft in a broad range of environments in three regions: the tropical Atlantic Ocean in winter, the Sonoran Desert under monsoon flow, and the arid high plains of Wyoming in summer. The main conclusions are as follows:

- 1) Cumuli are generally marked by a buoyant core, rising motion, and upper-level divergence. The flow

- patterns and buoyancy distribution near the cloud top suggest a toroidal ring circulation.
- 2) The cloud margin (roughly within 200 m on both sides of the cloud edge, or, in normalized space, roughly within 10% of the cloud diameter from the cloud edge) is characterized by sinking and downward accelerating flow, relatively cold air, and a rapid decay of liquid water content and droplet concentration toward the cloud edge. Composite evidence suggests that this subsidence is locally forced by evaporative cooling in entraining and detrainning eddies, although the cloud margin is characterized more by a minimum in buoyancy flux than a minimum of buoyancy itself. The typical lateral entrainment depth of eddies appears to be at most ~ 700 m.
- Geerts, B., Q. Miao, and J. C. Demko, 2008: Pressure perturbations and upslope flow over a heated, isolated mountain. *Mon. Wea. Rev.*, **136**, 4272–4288.
- Gerber, H., B. G. Arends, and A. S. Ackerman, 1994: New micrometeorology sensor for aircraft use. *Atmos. Res.*, **31**, 235–252.
- , G. Frick, J. B. Jensen, and J. G. Hudson, 2008: Entrainment, mixing, and micrometeorology in trade-wind cumulus. *J. Meteor. Soc. Japan*, **86A**, 87–106.
- Grabowski, W. W., 1993: Cumulus experiment, fine-scale mixing and buoyancy reversal. *Quart. J. Roy. Meteor. Soc.*, **119**, 935–956.
- , and T. L. Clark, 1993: Cloud-environment interface instability. Part II: Extension to three spatial dimensions. *J. Atmos. Sci.*, **50**, 555–573.
- Heus, T., and H. J. J. Jonker, 2008: Subsiding shells around shallow cumulus clouds. *J. Atmos. Sci.*, **65**, 1003–1018.
- , G. van Dijk, H. J. J. Jonker, and H. E. A. Van den Akker, 2008: Mixing in shallow cumulus clouds studied by Lagrangian particle tracking. *J. Atmos. Sci.*, **65**, 2581–2597.
- , C. F. J. Pols, H. J. J. Jonker, H. E. A. Van den Akker, and D. H. Lenschow, 2009: Observational validation of the compensating mass flux through the shell around cumulus clouds. *Quart. J. Roy. Meteor. Soc.*, **135**, 101–112.
- Houze, R. A., 1993: *Cloud Dynamics*. Academic Press, 573 pp.
- Hozumi, K., T. Harimaya, and C. Magono, 1982: The size distribution of cumulus clouds as a function of cloud amount. *J. Meteor. Soc. Japan*, **60**, 691–699.
- Jonas, P. R., 1990: Observations of cumulus cloud entrainment. *Atmos. Res.*, **25**, 105–127.
- Jonker, H. J. J., T. Heus, and P. P. Sullivan, 2008: A refined view of vertical mass transport by cumulus convection. *Geophys. Res. Lett.*, **35**, L07810, doi:10.1029/2007GL032606.
- Khairoutdinov, M., C. DeMott, and D. Randall, 2008: Evaluation of the simulated interannual and subseasonal variability in an AMIP-style simulation using the CSU multiscale modeling framework. *J. Climate*, **21**, 413–431.
- King, W. D., C. T. Maher, and G. A. Hepburn, 1981: Further performance tests on the CSIRO liquid water probe. *J. Appl. Meteor.*, **20**, 195–202.
- Krueger, S. K., C.-W. Su, and P. A. McMurtry, 1997: Modeling entrainment and finescale mixing in cumulus clouds. *J. Atmos. Sci.*, **54**, 2697–2712.
- Lenschow, D., E. Miller, and R. Friesen, 1991: A three-aircraft intercomparison of two types of air motion measurement systems. *J. Atmos. Oceanic Technol.*, **8**, 41–50.
- Lin, X., and R. H. Johnson, 1996: Heating, moistening, and rainfall over the western Pacific warm pool during TOGA COARE. *J. Atmos. Sci.*, **53**, 3367–3383.
- Lopez, R. E., 1977: The lognormal distribution and cumulus cloud populations. *Mon. Wea. Rev.*, **105**, 865–872.
- Paluch, I. R., 1979: The entrainment mechanism in Colorado cumuli. *J. Atmos. Sci.*, **36**, 2467–2478.
- , and C. A. Knight, 1984: Mixing and the evolution of cloud droplet size spectra in a vigorous continental cumulus. *J. Atmos. Sci.*, **41**, 1801–1815.
- Raga, G. B., J. B. Jensen, and M. B. Baker, 1990: Characteristics of cumulus band clouds off the coast of Hawaii. *J. Atmos. Sci.*, **47**, 338–356.
- Rauber, R., and Coauthors, 2007: Rain in shallow cumulus over the Ocean: The RICO campaign. *Bull. Amer. Meteor. Soc.*, **88**, 1912–1928.
- Rodts, S. M. A., P. G. Duynkerke, and H. J. J. Jonker, 2003: Size distributions and dynamical properties of shallow cumulus

REFERENCES

- Abel, S. J., and B. J. Shipway, 2007: A comparison of cloud-resolving model simulations of trade wind cumulus with aircraft observations taken during RICO. *Quart. J. Roy. Meteor. Soc.*, **133**, 781–794.
- Albrecht, B. A., C. W. Fairall, D. W. Thomson, A. B. White, J. B. Snider, and W. H. Schubert, 1990: Surface-based remote sensing of the observed and the adiabatic liquid water content of stratocumulus clouds. *Geophys. Res. Lett.*, **17**, 89–92.
- Blyth, A. M., 1993: Entrainment in cumulus clouds. *J. Appl. Meteor.*, **32**, 626–641.
- Brenguier, J., D. Baumgardner, and B. Baker, 1994: A review and discussion of processing algorithms for FSSP concentration measurements. *J. Atmos. Oceanic Technol.*, **11**, 1409–1414.
- Carbone, R. E., J. D. Tuttle, D. A. Ahijevych, and S. B. Trier, 2002: Inferences of predictability associated with warm season precipitation episodes. *J. Atmos. Sci.*, **59**, 2033–2056.
- Carpenter, R. L., K. K. Droegemeier, and A. M. Blyth, 1998: Entrainment and detrainment in numerically simulated cumulus congestus clouds. Part III: Parcel analysis. *J. Atmos. Sci.*, **55**, 3440–3455.
- Damiani, R., G. Vali, and S. Haimov, 2006: The structure of thermals in cumulus from airborne dual-Doppler radar observations. *J. Atmos. Sci.*, **63**, 1432–1450.
- , and Coauthors, 2008: Cumulus photogrammetric, in-situ and Doppler observations: The CuPIDO 2006 experiment. *Bull. Amer. Meteor. Soc.*, **89**, 57–73.
- Doswell, C. A., and P. M. Markowski, 2004: Is buoyancy a relative quantity? *Mon. Wea. Rev.*, **132**, 853–863.
- Frank, W. M., H. Wang, and J. L. McBride, 1996: Rawinsonde budget analyses during the TOGA COARE IOP. *J. Atmos. Sci.*, **53**, 1761–1780.

- clouds from aircraft observations and satellite data. *J. Atmos. Sci.*, **60**, 1895–1912.
- Sengupta, S. K., R. M. Welch, M. S. Navar, T. A. Berendes, and D. W. Chen, 1990: Cumulus cloud field morphology and spatial patterns derived from high-resolution Landsat imagery. *J. Appl. Meteor.*, **29**, 1245–1267.
- Siebesma, A. P., and Coauthors, 2003: A large eddy simulation intercomparison study of shallow cumulus convection. *J. Atmos. Sci.*, **60**, 1201–1219.
- Spyers-Duran, P. A., and D. Baumgardner, 1983: In flight estimation of the time response of airborne temperature sensors. Preprints, *Fifth Symp. on Meteorological Observations and Instrumentation*, Toronto, ON, Canada, Amer. Meteor. Soc., 352–357.
- Stull, R. B., 1988: *An Introduction to Boundary-Layer Meteorology*. Kluwer Academic Publishers, 670 pp.
- Wang, Y., and B. Geerts, 2009: Estimating the evaporative cooling bias of an airborne reverse flow thermometer. *J. Atmos. Oceanic Technol.*, **26**, 3–21.
- Warner, J., 1955: The water content in cumuliform cloud. *Tellus*, **7**, 449–457.
- Weckwerth, T. M., and Coauthors, 2004: An overview of the International H₂O Project (IHOP_2002) and some preliminary highlights. *Bull. Amer. Meteor. Soc.*, **85**, 253–277.
- Wielicki, B. A., and R. M. Welch, 1986: Cumulus cloud properties derived using Landsat satellite data. *J. Climate Appl. Meteor.*, **25**, 261–276.
- Yuter, S., and R. A. Houze, 1995: Three-dimensional kinematic and microphysical evolution of Florida cumulonimbus. Part II: Frequency distributions of vertical velocity, reflectivity, and differential reflectivity. *Mon. Wea. Rev.*, **123**, 1941–1963.
- Zhao, M., and P. H. Austin, 2005a: Life cycle of numerically simulated shallow cumulus clouds. Part I: Transport. *J. Atmos. Sci.*, **62**, 1269–1290.
- , and —, 2005b: Life cycle of numerically simulated shallow cumulus clouds. Part II: Mixing dynamics. *J. Atmos. Sci.*, **62**, 1291–1310.